Noninvasive Volumetric Imaging of Cardiac Electrophysiology

Linwei Wang[1], Heye Zhang[2], Ken C.L. Wong[1], Huafeng Liu [3], and Pengcheng Shi [1]
[1]Computational Biomedicine Laboratory, Rochester, NY, USA
maomaowlw@mail.rit.edu
[2]Bioengineering Instiute, University of Auckland, Auckland, Austrialia
[3]State Key Laboratory of Modern Optical Instrumentation, Zhejiang University, China

Abstract

Volumetric details of cardiac electrophysiology, such as transmembrane potential dynamics and tissue excitability of the myocardium, are of fundamental importance for understanding normal and pathological cardiac mechanisms, and for aiding the diagnosis and treatment of cardiac arrhythmia. Noninvasive observations, however, are made on body surface as an integration-projection of the volumetric phenomena inside patient's heart. We present a physiological-model-constrained statistical framework where prior knowledge of general myocardial electrical activity is used to guide the reconstruction of patient-specific volumetric cardiac electrophysiological details from body surface potential data. Sequential data assimilation with proper computational reduction is developed to estimate transmembrane potential and myocardial excitability inside the heart, which are then utilized to depict arrhythmogenic substrates. Effectiveness and validity of the framework is demonstrated through its application to evaluate the location and extent of myocardial infract using real patient data.

1. Introduction

Advances in medical imaging and computer vision have substantially improve the assessment of cardiac mechanical functions. Modern cardiac imaging modalities are able to produce noninvasive structural and kinematic observations of the 3D heart. From these images, global function measures such as cardiac output can be derived based on segmentation and shape representation of the ventricles [12, 4]. 3D motion and deformation of the heart wall can be reconstructed [15, 32]. These kinematic measures can be further related to actual cardiac mechanics, such as the distribution of strain, stress and material properties in the heart [17, 27].

Since cardiac mechanical function is triggered by cardiac electrical activity [21], volumetric electrophysiological details of the heart, such as transmembrane potential (TMP) dynamics and tissue excitability, are of fundamental importance for identifying origins responsible for pathological functions (arrhythmogenic substrates) and therefore improving treatment of cardiac arrhythmia.

However, standard noninvasive functional images of cardiac electrical activity are provided by body surface potential maps (BSPM), which are limited in spatial resolution and remote from the heart. Moreover, as defined by the quasi-static electromagnetic theory [24], they describe the integration of volumetric electrical activity of the heart but not the three-dimensionally distributed internal details.

Efforts in reconstructing cardiac electrophysiological details from BSPM mostly focus on electrical activity. Since electrical sources inside the myocardium cannot be uniquely determined from BSP distribution [33], most reconstructions are confined to equivalent physical models of cardiac sources [26] or TMP on heart surfaces [18]. To estimate unique TMP dynamics inside the myocardium, prior physiological knowledge about volumetric TMP activity is needed to constrain the solution space [16]. Because prior knowledge of general population is different from specific conditions of individual subjects, and BSPM data are always noise-corrupted, a proper combination of the information in prior knowledge and patient's BSPM should take into account these uncertainties. We have developed a a physiological-model-constrained statistical framework for volumetric TMP imaging using noninvasive BSPM [29]. However, when applied to myocardial infarction, such framework relies only on the abnormality of estimated TMP dynamics without considering the inherent myocardial viability.

In this paper, we further develop the physiological-model-constrained statistical framework for imaging complete cardiac electrophysiology, including TMP dynamics and tissue excitability. Firstly, the cardiac electrophysiological system is modeled on specific heart-torso structures derived from patient's tomographic images. In this system, general physiological knowledge about TMP activity is

978-1-4244-3991-1/09/$25.00 ©2009 IEEE

contained in the volumetric myocardial TMP activity model with parameters representing tissue excitability of the myocardium. The TMP-to-BSP model describes the imaging process of obtaining BSPM from TMP. This system is reformulated into a stochastic state space representation to take into account model and data errors. Sequential data assimilation with proper computational reduction is developed for estimating TMP and/or tissue excitability in the heart. These estimates are further utilized for imaging of arrhythmogenic substrates.

The presented framework is applied to real patient data on myocardial infarction (MI) for imaging the volumetric conduction abnormality caused by the infarct and tissue excitability of the myocardium. It also depicts the distribution of infarct substrate inside the patient's heart, and shows improved infarct evaluation over existent works. These promising results demonstrate the capability of the presented framework in providing noninvasive volumetric imaging of cardiac electrophysiology.

2. Cardiac Electrophysiological Dynamics and Observations

Cardiac electrical activity exhibits as the spatiotemporal TMP dynamics inside the heart, and produces noninvasive observations on the body surface. The cardiac electrophysiological system is modeled to incorporate these physiological knowledge on personalized heart and torso structures, so that they can be used to constrain the BSPM-driven imaging of patient-specific cardiac electrophysiology.

2.1. Persnoalized Heart-Torso Representation

After segmenting a set of short-axis cardiac MRI and building a smoothed mesh for the heart surfaces [28], the 3D heart wall is represented by dropping point cloud (meshfree points) inside the surface mesh. Myocardial conductive anisotropy is considered by mapping volumetric fiber structures from the standard mathematical model of fibrous structure developed in [23]. Heterogeneity of TMP shapes in the epi-, endo- and mid-myocardial regions [34] is also taken into account. Because torso geometry is the primary factor affecting TMP-to-BSP relationship [5], the torso is assumed as an isotropic and homogeneous volume conductor described by triangulated body surface. It is obtained by deforming a reference torso model to match patient's image data [7]. In practice, 2000 to 5000 meshfree points and 300 to 1000 vertices on body surface are used for a physiological plausible yet computational feasible representation [3].

2.2. Volumetric TMP Dynamics

Myocardial TMP dynamics is described by the 2-variable diffusion-reaction system from [1] for the balance between model plausibility and computational feasibility:

$$\begin{cases} \frac{\partial u}{\partial t} = \nabla \cdot (\mathbf{D}\nabla u) + ku(u-a)(1-u) - uv \\ \frac{\partial v}{\partial t} = -e(v + ku(u-a-1)) \end{cases} \tag{1}$$

where u stands for TMP and v for recovery current. $\mathbf{D}$ is the diffusion tensor and $\nabla \cdot (\mathbf{D}\nabla u)$ accounts for the electrical propagation. Parameters e, k and a determine individual TMP shapes, where a represents the tissue excitability of the myocardium. With the meshfree method [35], TMP activity model in patient's heart is developed from (1) as:

$$\begin{cases} \frac{\partial \mathbf{U}}{\partial t} = -\mathbf{M}^{-1}\mathbf{K}\mathbf{U} + k\mathbf{U}(\mathbf{U}-a)(1-\mathbf{U}) - \mathbf{U}\mathbf{V} \\ \frac{\partial \mathbf{V}}{\partial t} = -e(\mathbf{V} + k\mathbf{U}(\mathbf{U}-a-1)) \end{cases} \tag{2}$$

where vectors $\mathbf{U}$ and $\mathbf{V}$ consist of u and v from all meshfree points. Matrices $\mathbf{M}$ and $\mathbf{K}$ encode 3D myocardial structure and its conductive anisotropy. Variations of a across the heart wall produce the transmural electrical heterogeneity.

Volumetric TMP dynamics and myocardial tissue excitability contain important electrophysiological information, which further imply the property of arrhythmogenic substrates. For example, late activation time and reduced TMP duration constitute the characteristics for infarcted tissues; the activation origin beside normal pacemakers points to the ectopic foci; and the asynchronized activation of the ventricles indicate the blocks in bundle branches. Tissue excitability further provides a direct picture of the pathophysiological condition of the myocardium. For instance, areas with abnormally higher or lower excitability indicate the existence of accessory pathways or infarcted tissues respectively.

2.3. TMP-to-BSP Mapping

Noninvasive observations of myocardial TMP dynamics are recorded as potential differences on the body surface. This relationship between volumetric TMP and BSPM follows the quasi-static electromagnetism [24] on the personalized heart-torso model. With the assumption of anisotropic intracellular electrical conductivity $\mathbf{D}_i$ and isotropic torso conductivity σ, distribution of potential ϕ within the homogeneous torso Ω_t is governed by a Poisson equation:

$$\sigma\nabla^2\phi(\mathbf{r}) = \nabla \cdot (-\mathbf{D}_i(\mathbf{r})\nabla u(\mathbf{r})) \qquad \forall \mathbf{r} \in \Omega_t \tag{3}$$

Combing the meshfree and boundary element method (BEM) to solve (3), we obtain the linear relationship between volumetric TMP and BSP:

$$\mathbf{\Phi} = \mathbf{H}\mathbf{U} \tag{4}$$

where $\mathbf{\Phi}$ consist of ϕ from all vertices on the body surface. This model combines the advantage of existent FEM-based [10] and BEM-based [11] approach to TMP-to-BSP modeling, allowing the investigation of volumetric TMP in the heart while avoiding irrelevant variables to reduce model complexity [30].

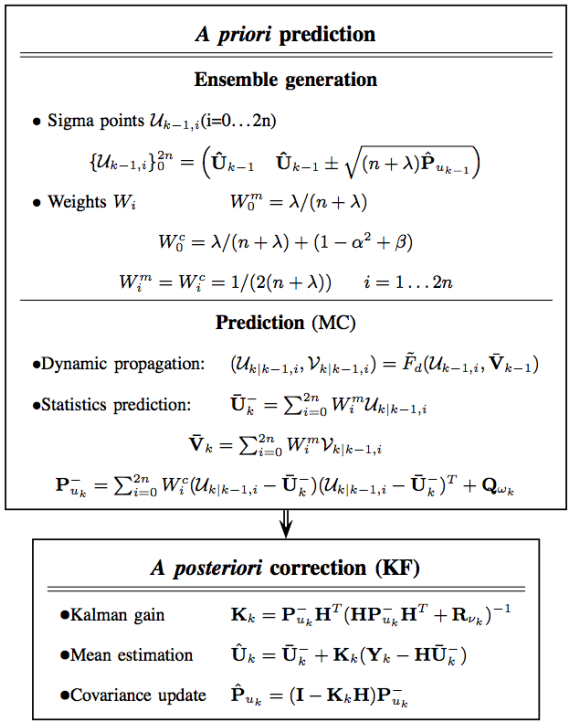

Figure 1. Flow of TMP estimation algorithm from instant $k-1$ to k, where a specific $2n+1$ sigma point set is used as an example. n: dimension of $\mathbf{U}$. $\mathbf{Q}_{\omega_k}$ and $\mathbf{R}_{\nu_k}$: pre-specified covariance matrices for ω_k and ν_k. α, β and λ: parameters determined according the unscented transform [19].

3. Noninvasive Volumetric Imaging of Cardiac Electrophysiology

Because $\mathbf{U}$ is of much larger dimension than $\mathbf{\Phi}$, (4) is an underdetermined linear system. Furthermore, because the condition number of $\mathbf{H}$ is usually at a magnitude of 10^{16}, small perturbations in $\mathbf{\Phi}$ could lead to wild fluctuations in $\mathbf{U}$. This explains why physiological constraints are needed to reduce the solution space for unique $\mathbf{U}$ from $\mathbf{\Phi}$. In patient-specific cardiac electrophysiological imaging, however, these model-contained knowledge introduce errors caused by inaccurate model parameters and imprecise model structures. Meanwhile, data errors are unavoidable in tomographic images and BSPM. To explicitly account for these uncertainties, the physiological system (2, 4) is reformulated into state space representations. Sequential data assimilation with proper computational reduction is developed for TMP estimation, or simultaneous TMP and excitability estimation. Arrhythmogenic substrates are further identified from these estimates.

3.1. Imaging Volumetric TMP Dynamics

By letting the state vector $\mathbf{X}(t) = \left(\mathbf{U}(t)^T \mathbf{V}(t)^T\right)^T$, the volumetric myocardial TMP activity model (2) corresponds to the state equation with an additive stochastic component $\omega(t)$ accounting for model uncertainties:

$$\frac{\partial \mathbf{X}(t)}{\partial t} = F(\mathbf{X}(t)) + \omega(t) \tag{5}$$

where $F(\mathbf{X}(t))$ is rearranged from (2). Accordingly, with the measurement vector $\mathbf{Y}(t) = \mathbf{\Phi}(t)$, the TMP-to-BSP model (4) becomes the measurement equation with an additive noise $\nu(t)$ accounting for model and data errors:

$$\mathbf{Y}(t) = \begin{pmatrix}\mathbf{H} & \mathbf{0}\end{pmatrix} \mathbf{X}(t) + \nu(t) = \tilde{\mathbf{H}}\mathbf{X}(t) + \nu(t) \tag{6}$$

This continuous system (5,6) is temporally discretized according to the BSPM sampling instants:

$$\mathbf{X}_k = F_d(\mathbf{X}_{k-1}) + \omega_k \tag{7}$$
$$\mathbf{Y}_k = \tilde{\mathbf{H}}\mathbf{X}_k + \nu_k \tag{8}$$

where a Runge-Kutta solver is used to solve (5) and no explicit formulation exists for $\mathbf{F}_d$.

Given patient's BSPM sequence, volumetric TMP can be estimated by sequential data assimilation [2] with fixed parameters in the state space equations. Because the nonlinear TMP activity model (2) does not allow easy local linearization or temporal discretization, it is improper to apply the widely-used Kalman filter (KF) or extended KF [2] to this system. Meanwhile, because this system is of large scale, high dimensionality and intricate structure, the alternative Monte Carlo (MC) methods [25] are impractical due to the intensive computation. In order to preserve the intact model nonlinearity and maintain computational feasibility, the TMP estimation algorithm is developed based on the recently presented unscented KF (UKF) [20] to combine the advantages of MC methods and KF updates.

Since $\mathbf{V}$ is not of interest to our problem and its change is not directly reflected in BSPM, we avoid the estimation of $\mathbf{V}$ so as to reduce the dimension of the unknowns. The TMP estimation algorithm is composed of temporal iterations as described in Fig 1. At each time step k, a set of l samples (sigma points) $\{\mathcal{U}_{k-1,i}\}_{i=1}^{l}$ is generated from the previous estimates of mean $\hat{\mathbf{U}}_{k-1}$ and error covariance $\hat{\mathbf{P}}_{u_{k-1}}$ according to the deterministic mechanism of unscented transform [19]. Each sigma point $\mathcal{U}_{k-1,i}$ is transformed through the deterministic state model with the same vector $\bar{\mathbf{V}}_{k-1}$ to generate two new ensemble sets $\{\mathcal{U}_{k|k-1,i}\}_{i=1}^{l}$ and $\{\mathcal{V}_{k|k-1,i}\}_{i=1}^{1l}$. $\{\mathcal{U}_{k|k-1,i}\}_{i=1}^{l}$ is used to predict $\mathbf{U}_k^-$ and $\mathbf{P}_{u_k}^-$ using MC integration, and estimates of $\hat{\mathbf{U}}_k$ and $\hat{\mathbf{P}}_{u_k}$ are obtained from KF update rules. Meanwhile, $\bar{\mathbf{V}}_k$ is calculated from $\{\mathcal{V}_{k|k-1,i}\}_{i=1}^{l}$ for the next iteration. Initialized with $\hat{\mathbf{U}}_0$ and $\hat{\mathbf{P}}_{u_0}$, such iteration continues at each BSPM sampling instant in the cardiac cycle.

3.2. Imaging Tissue Excitability of the Myocardium

Tissue excitability of the myocardium is imaged by estimating a in (1) in addition to TMP. By setting a as unknown, we augment the original state vector into $\mathbf{X}^a(t) = \left(\mathbf{U}(t)^T\mathbf{V}(t)^T\mathbf{\Psi}^T\right)^T$, where $\mathbf{\Psi}$ includes a on all meshfree points. Assuming that tissue excitability varies slowly in time, we have:

$$\mathbf{\Psi}_k = \mathbf{\Psi}_{k-1} + \omega_{\Psi_k} \tag{9}$$

Simultaneous estimation of $\mathbf{U}$ and $\mathbf{\Psi}$ is done by loosely coupling another *excitability estimator* to the *TMP estimator* (dual estimation). At time step k, we have TMP estimates $\hat{\mathbf{U}}_{k-1}$, $\hat{\mathbf{P}}_{u_{k-1}}$ and excitability estimates $\hat{\mathbf{\Psi}}_{k-1}$, $\hat{\mathbf{P}}_{\Psi_{k-1}}$. Firstly, the excitability estimator utilizes $\hat{\mathbf{U}}_{k-1}$ to update $\mathbf{\Psi}_k$ (Fig 2.) : a set of l sigma points $\{\ominus_{k-1,i}\}_{i=1}^{l}$ is generated from $\hat{\mathbf{\Psi}}_{k-1}$ and $\hat{\mathbf{P}}_{\Psi_{k-1}}$. $\{\ominus_{k-1,i}\}_{i=1}^{l}$ is passed through the TMP activity model with $\hat{\mathbf{U}}_{k-1}$ to generate a new ensemble set $\{\mathcal{U}^{\Psi}_{k|k-1,i}\}_{i=1}^{l}$, which is further propagated through the TMP-to-BSP model to generate $\{\mathcal{Y}^{\Psi}_{k,i}\}_{i=1}^{l}$. These ensemble sets are used to get estimates of $\hat{\mathbf{\Psi}}_k$, $\hat{\mathbf{P}}_{\Psi_k}$ using KF update rules. The updated $\hat{\mathbf{\Psi}}_k$ is then used in the TMP estimator for estimating $\hat{\mathbf{U}}_k$ and $\hat{\mathbf{P}}_{u_k}$.

To improve computational efficiency, the frequency of excitability estimation can be reduced. For example, it can be evoked after every m iterations of TMP estimation, or only when the discrepancy between model-generated and patient's BSPM is over predefined thresholds. Fig 3 illustrates the schematic of this dual-estimator. In practice, it is desirable to initialize this estimator with a close approximation of tissue excitability distribution. Such knowledge can be provided by the TMP imaging results from section 3.1.

3.3. Computational Reduction

The TMP estimation (Fig 1) requires l model simulation for passing the sigma point set through the TMP activity model. Since l is usually proportional to the dimension of $\mathbf{U}$, it leads to expensive computation. For simultaneous estimation of excitability, the computation is further doubled.

The key for reducing computational time is to cut down the number of sigma points used in the filtering. Since the set of sigma points is used to approximate the probabilistic distribution characterized by mean and error covariance, its size can be reduced by considering only the dominant components of error covariances. This is done by replacing the error covariance $\mathbf{P}$ with its rank-q SVD $\mathbf{P}^q = \mathbf{V}^q\mathbf{D}^q\mathbf{V}^{qT}$, where $\mathbf{D}^q$ contains the first q leading eigenvalues and $\mathbf{V}^q$ the corresponding eigenvectors. Meanwhile, to avoid filtering divergence, the square root (SR) structure is unified with the reduced-rank (RR) filtering by defining the SR of $\mathbf{P}$ as $\mathbf{S}^q = \mathbf{V}^q\sqrt{\mathbf{D}^q}$. We develop the integrated RRSR filtering [31] and apply it to the TMP and excitability estimators to improve their computational efficiency and stability.

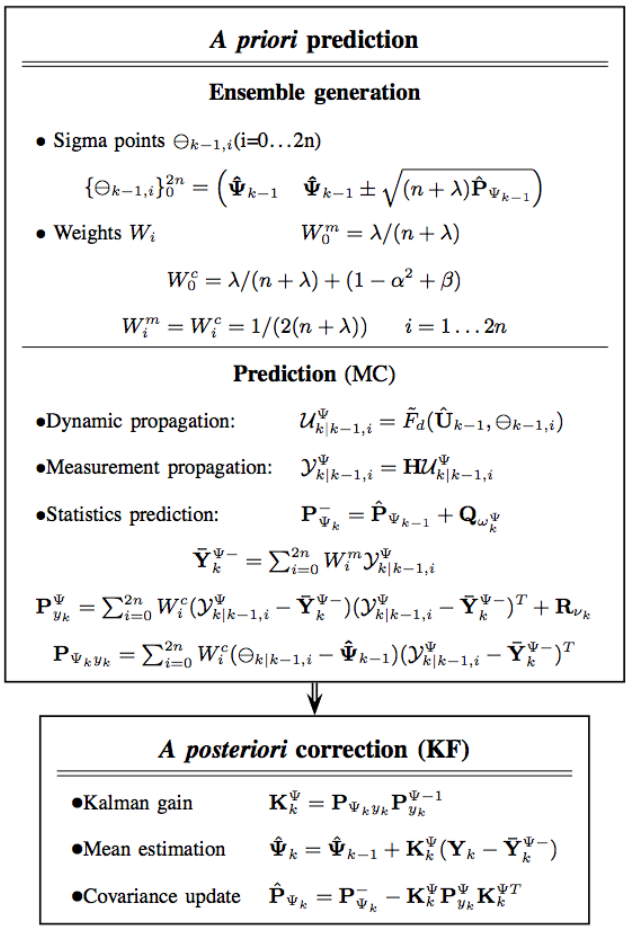

Figure 2. Flow of excitability estimation algorithm from instant $k-1$ to k. $\mathbf{Q}_{\omega_k^{\Psi}}$: pre-specified covariance matrices for ω_k^{Ψ}.

4. Experiments

The presented framework are applied on 4 sets of MRI and BSP data collected from patients with acute MI [13], and here we discuss the details of one set of results in imaging the abnormal volumetric conduction, tissue excitability and infarct substrate inside the patient's heart. The cardiac MRIs contain 9 slices from apex to base, with 8mm interslice spacing and 1.33mm/pixel in-plane resolution. Each BSPM is recorded from 123 electrodes and interpolated to 370 nodes on the torso surface, and the sequence consists of a single averaged PQRST complex sampled at 2k Hz. Anatomical locations of all electrodes and nodes are available. Fig 4 (a) illustrates the combined heart-torso model of the patient, where the torso is represented by triangulated body surface with 370 vertices and the 3D ventricular mass by a cloud of 1230 meshfree points with detailed fiber structure. Fig 4 (b) exemplifies an input BSPM.

There are gold standards of volumetric TMP activity or conductivity available. Instead, we are provided with reference interpretation of the infarct substrate from cardiolo-

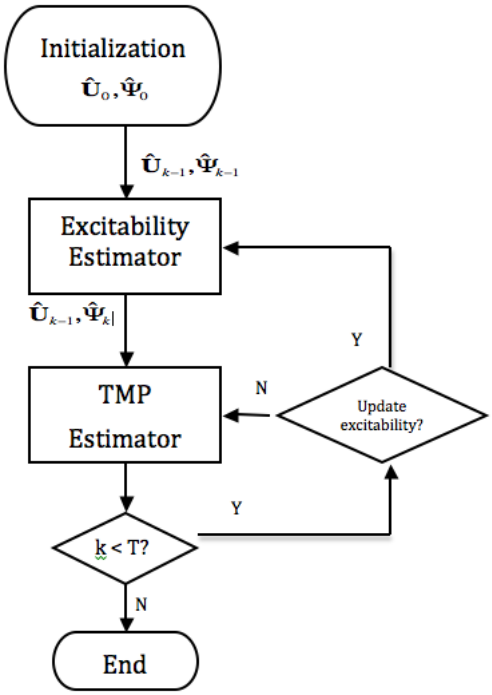

Figure 3. Dual estimator for simultaneous volumetric excitability and TMP imaging. T: total number of estimation steps.

gists who examined the gadolinium enhanced images of the heart. This evaluation, based on the standard 17-segment division of LV (Fig 6) [6], identifies the percentage of infarcted myocardial mass ($EP = 52\%$), the segment containing the centroid of infarcted substrates ($CE = 10$ or 11) and all infarcted segments (3-5, 9-12, 15-16). In other words, the infarct substrate is distributed in the inferior-lateral LV with its center in the middle layer. Meanwhile, some efforts provided evaluation of the infarct substrate on the same data set. Comparisons of the infarct imaging with the reference interpretation and existent results provide the quantitative validation of the presented framework.

4.1. Volumetric Cardiac Electrophysiological Imaging

Fig 5 (b) lists the final imaging results of the volumetric TMP dynamics in patient' heart. Compared to the TMP activity obtained by simulating normal conditions in the patient's heart (Fig 5 (a)), the reconstructed TMP exhibits distinct conduction delay and block in the inferior part of basal-middle LV and lateral part of middle-apical LV, which is in accordance with true infarct location.

Imaging of tissue excitability is initialized according to this TMP estimates, where the LV area with abnormally late activation time are assigned with lower excitability (larger value of a) than the remaining myocardium. Fig 7 depicts tissue excitability in patient's heart, exhibiting a low-

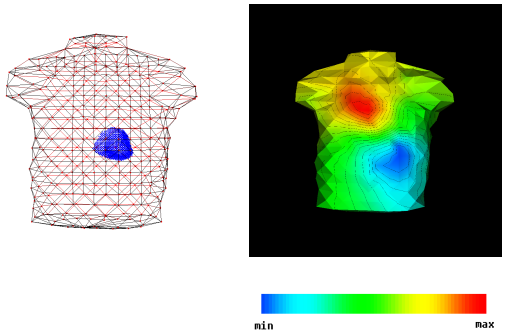

(a) (b)

Figure 4. (a) Patient-sepcific combined heart-torso model, where the ventricles are represented with a cloud of 1230 meshfree points and the torso by triangulated body surface with 370 vertices. (b) Exemplary input BSPM at 85ms of ventricular activation, the color bar encoding BSP magnitude.

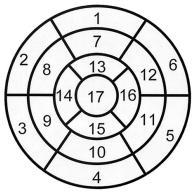

Figure 6. Standard 17-segement division of LV wall (polor map). Segments $1-6$ lie in the basal layer, $7-12$ in the middle layer, $13-16$ in the apical layer and 17 is the apex. At each layer, the segment labeling moves from anterior, septal, inferior to lateral part of the LV.

excitability zone located in the LV area which is identified as infarcted by reference interpretation. Meanwhile, from estimated temporal TMP shape at each meshfree points, the activation time and TMP duration is calculated (Fig 8 (b)). Their weighted combination is used to produce the infarct metric M_i ($0 \leq M_i \leq 1$) in a way that meshfree points with later activation time and shorter TMP duration would have M_i closer to 1. Fig 9 pictures the distribution of infarct substrate based on the value of M_i. As shown, the area highlighted as the infarct substrate (with evidently higher M_i value) is again consistent with the reference interpretation, and has large overlaps with the low-excitability zone identified in Fig 7. A more complete investigation of the correlation of such abnormality between TMP and excitability is to be conducted in future study.

4.2. Quantitative Validation

In evaluating the quantitative infarct parameters, the center of the infarct substrate CE is located as the center of all infarcted meshfree points weighted by M_i. EP is obtained by dividing the number of infarcted meshfree points by the total number of meshfree points. The overlap of the identified infarcted segments with the reference interpretation

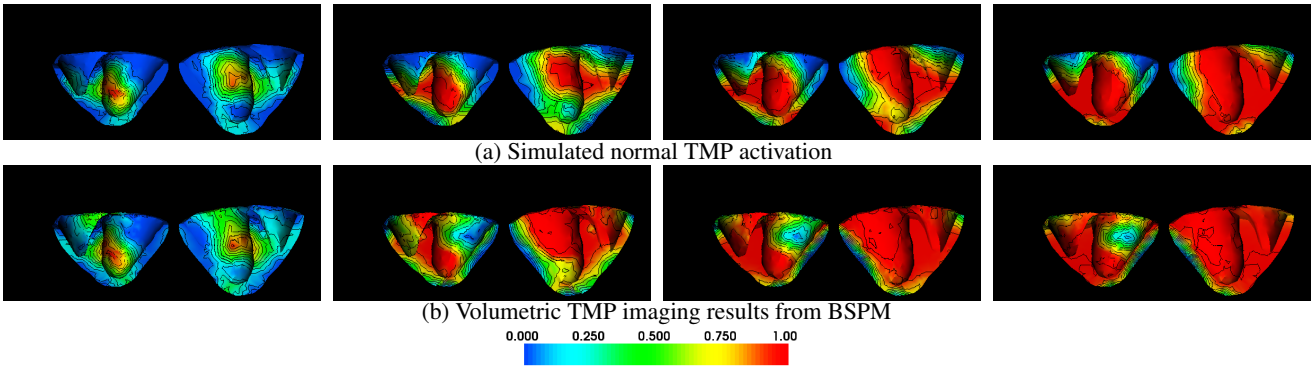

(a) Simulated normal TMP activation

(b) Volumetric TMP imaging results from BSPM

Figure 5. Volumetric myocardial TMP imaging during ventricular activation of the patient with MI. The color bar encodes normalized TMP values. Left to right in (a) and (b) 35, 64, 78, 89ms after the onset of ventricular activation.

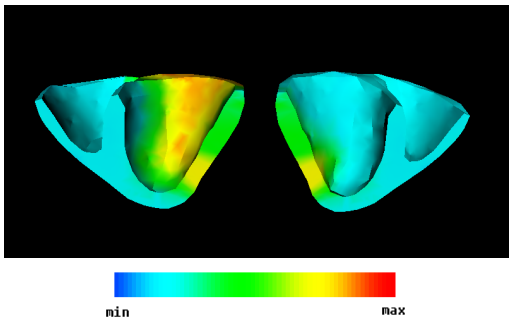

Figure 7. Imaging of tissue excitability of the myocardium, where the color bar encodes the value of parameter a (higher value of a corresponds to lower excitability). Abnormally lower excitability is exhibited in the inferior part of basal-middle LV and lateral part of middle-apical LV.

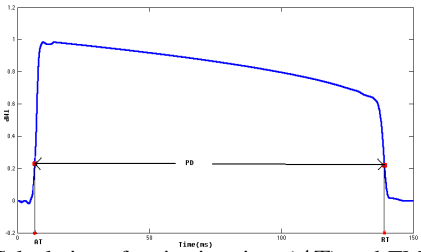

Figure 8. Calculation of activation time (AT) and TMP duration (PD) from temporal TMP shape, where AT is determined as the point with the largest positive derivative.

(SO) measures the percentage of correct identification.

Table 1 compares these results with the reference interpretation and 3 other existent results on the same data set. In brief, results from Dawoud *et al* were based on the epicardial potential imaging from BSPM [8], results of Farina *et al* came from deterministic optimization of the heart model using BSPM [9], and Mneimneh *et al* produced the best existent results using simple ECG signal analysis [22]. As shown by the CE and SO, our results are close to the reference interpretation, comparable to the

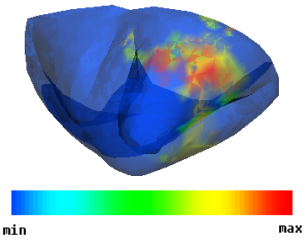

Figure 9. Imaging of the infarct substrate based on TMP estimates, where the color bar encodes the value of infarct metric M_i (higher value of M_i indicates more severe infarction). The substrate is distributed in the inferior part of basal-middle LV and lateral part of the apical-middle LV, which largely overlap with the low-excitaility area in Fig 7.

best results and substantially improved over the other two electrophysiological-imaging approaches. The EP in our results is again close to the best results. Because the reference interpretation identifies the substrate by segments, its EP only measures the percentage of affected segments in all 17 segments ($EP = 9/17 \simeq 52\%$). Instead, our approach provides improved precision by differentiating between normal and infarcted tissues within the same segment. It explains why our approach produces smaller EP than reference interpretation.

Fig 8 lists the imaging results of tissue excitability superimposed with localized TMP abnormality for the other 3 data sets. Detailed explanations are omitted because of space limits. In general, the presented framework is able to correctly localize infarct substrate as validated by gold standards for each case.

5. Conclusions and discussions

While the assessment of cardiac mechanical functions has been substantially improved by the advances in medical imaging and computer vision, the assessment of cardiac

Table 1. Comparison of MI evaluation results with the reference interpretation (the 2nd column) and existent best results (the 4th-6th columns). EP represents the percentage of identified infarcted tissues in the ventricular mass. SO measures the percentage of correct identification compared to the reference interpretation. CE is the segment containing the center of the infarct substrate, and $segments$ are identified as containing the infarct substrate.

	Reference	Our results	Mneimneh	Dawoud	Farina
EP	52%	28%	27%	35%	10%
SO	N/A	90%	90%	55.6%	40%
CE	10/11	11	10/11	4	12
segments	3-5,9-12,15-16	5,10-12,16	N/A	3-5,10,11	N/A

electrophysiology is relatively in its infancy. On one hand, the standard noninvasive functional images of cardiac electrical activity provided by BSPM lose volumetric details inside the heart. On the other, most existent efforts in noninvasive electrophysiological imaging are confined to reconstructing information about electrical activities and ignores inherent tissue properties of the heart.

Treatment of cardiac arrhythmia usually requires identification of arrhythmic details and arrhythmogenic substrates. Volumetric details of patient's cardiac electrophysiology, such as TMP dynamics, tissue excitability and arrhythmogenic substrates, are of great clinical importance. In this paper, we present a physiological-model-constrained statistical framework for volumetric imaging of all these electrophysiological information using noninvasive BSPM data. As demonstrated in the human study of MI, the presented framework is able to provide plausible volumetric imaging of patient's cardiac electrophysiology and improve identification of infarct substrates over existent works.

Modeling of the cardiac electrophysiological system provides sophisticated physiological constraints on reconstructing volumetric cardiac phenomena from BSPM. The level of modeling details has to maintain recosntructibility of TMP and/or tissue excitability given limited amount of information in input data, as well as computational feasibility with available computational resources. With increased information and resolution in patient's data, as well as more computational resources, this modeling can go into finer details and scales in the future.

In the presented state space systems, the widely-used assumption of additive model and data errors are adopted for simplification. Since the UKF is able to deal with uncertainties nonlinearly injected into the system models [20], future studies will extend to more generalized state space systems with more sophisticated uncertainty modeling.

The current study considers the tissue excitability because it is an essential electrophysiological property that directly exhibits pathophysiological conditions of the myocardium. Following the same line of simultaneous state and parameter estimation, imaging of other important electrophysiological properties is also feasible. For example, the diffusion tensor $\mathbf{D}$ in (1) is usually assumed as d diag$\{4, 1, 1\}$ with d proportional to electrical conductivity. The imaging of electrical conductivity in the heart, therefore, can be achieved by the dual estimation of d and TMP.

Beside dual estimation, simultaneous reconstruction of TMP and model parameters can also be done by joint estimation, where a single state estimator is applied to the augmented state space system. Compared to dual estimation, this strategy requires easier implementation. However, the degree of freedom in the augmented system is largely increased, making the estimation unstable especially with the nonlinear dynamic models [14]. A comparison of the performance of dual-estimator and joint-estimator in this problem deserves further investigation in future studies.

Regarding the tight cardiac electromechanical coupling [5], integration of patient's mechanical and electrical imaging data (such as MRI and BSPM) could improve the assessment of cardiac mechanics and electrophysiology. On one hand, the incorporation of structural images in addition to BSPM will enhance the patient-specificity of the volumetric imaging of patient's cardiac electrophysiology. On the other hand, including of BSPM will bring further progress to the assessment of cardiac mechanics. Future works will focus on the integration of noninvasive mechanical and electrical observations for a complete volumetric imaging of patient's cardiac electrophysiology and mechanics.

While this paper focus on the specific applications in cardiac electrophysiology, the fundamental system perspective behind the presented framework can be used to solve a large variety of real-world problems, based on the emphasis that 1), scientific knowledge contained in general models is used to guide the extraction of subject-specific information from observational data; 2), subject-specific information in the data is used to identify changed model parameters; and 3), these two sources of information are combined in a statistical perspective.

References

[1] R. R. Aliev and A. V. Panfilov. A simple two-variable model of cardiac excitation. *Chaos, Solitions & Fractals*, 7(3):293–301, 1996. 2

[2] B. D. Anderson and J. B. Moore. *Optimal Filtering*. Prentice-Hall, New Jersey, 1979. 3

[3] Authors. Coupled meshfree-bem platform for electrocardiographic simulation. Technical report, Supplied as supplementary material Modeling.pdf. 2

[4] L. Axel, A. Montillo, and D. Kim. Tagged magnetic resonace imaging of the heart: a survey. *Medical Image Analysis*, 9:376–393, 2005. 1

[5] C. P. Brandley, A. J. Pullan, and P. J. Hunter. Effects of material properties and geometry on electrocardiographic forward simulations. *Annals of Biomedical Engineering*, 28:721–741, 2000. 2, 7

[6] M. D. Cerqueira, N. J. Weissman, V. Dilsizian, A. K. Jacobs, S. Kaul, W. K. Laskey, D. J. Pennell, J. A. Rumberger, T. Ryan, and M. S. Verani. Standardized myocardial segmentation and nomenclature for tomographic imaging of the heart. *Circulation*, 105:539–542, 2002. 5

[7] L. Cheng. *Non-invasive Electrical Imaging of the Heartl*. PhD thesis, Univ. of Auckland, New Zealand, 2001. 2

[8] F. D. Dawoud. Using inverse electrocardiography to image myocardial infarction. In *Proc. Computers in Cardiology*. 6

[9] D. Farina. Model-based approach to the localization of infarction. In *Proc. Computers in Cardiology*. 6

[10] G. Fischer, B. Tilg, R. Modre, G. J. M. Huiskamp, J. Fetzer, W. Rucker, and P. Wach. A bidomain model based bem-fem coupling formulation for anisotropic cardiac tissue. *Annals of Biomedical Engineering*, 28:1229–1243, 2000. 2

[11] G. Fischer, B. Tilg, P. Wach, G. Lafter, and W. Rucker. Analytical validation of the bem-application of the bem to the electrocardiographic forward and inverse problem. *Computer Methods and Programs in Biomedicine*, 55:99–106, 1998. 2

[12] A. F. Frangi, W. J. Niessen, and M. A. Viergever. Three-dimensional modeling for functional analysis of cardiac images: A review. *IEEE Transactions on Medical Imaging*, 20(1):2–25, 2001. 1

[13] A. L. Goldberger et al. Physiobank, physiotoolkit, and physionet components of a new research resource for complex physiological signals. *Circulation*, 101:e215–e220, 2000. 4

[14] H. G. H. Moradkhani, S. Sorooshian and P. Houser. Dual state-parameter estimation of hydrological models using ensemble kalman filter. *Advances in Water Resources*, 28:135–147, 2005. 7

[15] I. Haber, D. Metaxas, and L. Axel. Three-dimensional motion reconstruction and analysis of the right ventricle using tagged mri. *Medical Image Analysis*, 4:335–355, 2000. 1

[16] B. He, G. Li, and X. Zhang. Noninvasive imaging of cardiac transmembrane potentials within three-dimensional myocardium by means of a realistic geometry aniostropic heart model. *IEEE Transactions on Biomedical Engineering*, 50:1190–1202, 2003. 1

[17] Z. Hu, D. Metaxas, and L. Axel. In vivo strain and stress estimation of the heart left and right ventricles from mri images. *Medical Image Analysis*, 7:435–444, 2003. 1

[18] G. Huiskamp and F. Greensite. A new method for myocardial activation imaging. *IEEE Transactions on Biomedical Engineering*, 44(6):446, 1997. 1

[19] S. J. Julier. The scaled unscented transform. In *Proc. American Control Conference*, pages 4555–4559, 2002. 3

[20] S. J. Julier and J. K. Uhlmann. A new extension of the kalman filter to nonlinear systems. In *Proc. Aerospace/Defense Sensing, Simulation and Controls*, pages 182–193, 1997. 3, 7

[21] A. McCulloch, J. Bassingthwaighte, P. Hunter, and D. Noble. Computational biology of the heart: From structure to function. *Progress in Biophysics and Molecular Biology*, 69:153–155, 1998. 1

[22] M. A. Mneimneh and R. J. Povinelli. Rps/gmm approach toward the localization of myocardial infarction. In *Proc. Computers in Cardiology*. 6

[23] M. Nash. *Mechanics and Material Properties of the Heart using an Anatomically Accurate Mathematical Model*. PhD thesis, Univ. of Auckland, New Zealand, May 1998. 2

[24] R. Plonsey. *Bioelectric phenonmena*. McGraw Hill, New York, 1969. 1, 2

[25] B. Ristic. *Beyond the Kalman Filter: Particle Filters for Tracking Applications*. Artech House, Boston,MA, 2004. 3

[26] Y. Rudy and B. Messinger-Rapport. The inverse problem of electrocardiography: solutions in terms of epicardial potentials. *Critical Reviews in Biomedical Engineering*, 16:215–268, 1988. 1

[27] M. Sermesant, P. Moireau, O. Camara, J. Sainte-Marie, R. Andriantsimiavona, R. Cimrman, D. L. Hill, D. Chapelle, and R. Razavi. Cardiac function estimation from mri using a heart model and data assimilation: advances and difficulties. *Medical Image Analysis*, 10:642–656, 2006. 1

[28] G. Taubin. Curve and surface smoothing without shrinkage. pages 825–857, 1995. 2

[29] L. Wang, K. Wong, H. Zhang, and P. Shi. Noninvasive functional imaging of volumetric cardiac electrical activity: A human study on myocardial infarction. In *Proc. Medical Image Computing and Computer Assisted Intervention (MICCAI '08)*, volume 1, pages 1042–1050, 2008. 1

[30] L. Wang, H. Zhang, K. Wong, H. Liu, and P. Shi. Electrocardiographic simulation on personalized heart-torso structures using coupled meshfree-bem platform. *International Journal of Functional Informatics and Personalized Medicine*, In press, 2009. 2

[31] L. Wang, H. Zhang, K. Wong, and P. Shi. Integrated reduced-rank square root unscented kalman filter for large scale data assimilation. *Signal Processing*, Under review, 2009. 4

[32] C. L. Wong, H. Y. Zhang, H. F. Liu, and P. C. Shi. Physiome-model-based state-space framework for cardiac deformation recovery. *Academic Radiology*, 14:1341–1349, 2007. 1

[33] Y. Yamashita. Theoretical studies on the inverse problem of electrocardiography and the uniqueness of the solution. *IEEE Transactions on Biomedical Engineering*, 29(11):719–725, 1982. 1

[34] G. X. Yan, W. Shimizu, and C. Antzelevitch. Charactertistics and distribution of m cells in arterially perfused canine left ventricular wedge preparations. *Circulation*, 98:1921–1927, 1998. 2

[35] H. Zhang and P. Shi. A meshfree method for solving cardiac electrical propagation. In *Proc. International Conference of the IEEE Engineering in Medicine and Biology Science*, pages 349 – 352, 2005. 2